Supporting Information

SI Methods

The Quadratic Echo Pulse Block. Our approach to the MRI of solids makes use of repeating blocks of pulses. All images in this paper used the quadratic echo pulse block in Fig. 1A, which is a second-generation modification of a particular first-generation pulse block. The theory underlying the design of the first-generation quadratic echo sequence and experiments demonstrating its effect (e.g., line-narrowing of the ^{29}Si spectrum by a factor of about 70,000), have been published (1–6). Here, we briefly review the key details.

This pulse block was designed to control a mesoscopic cluster of N spin $I = \frac{1}{2}$ nuclei (e.g., ^{31}P), with a spin Hamiltonian (in the rotating frame) of the form $H_{int} = H_Z + H_{ZZ}$, where the Zeeman term $H_Z = \sum_i^N \Omega_{z_i}^{net} I_{z_i} = \Omega_z^{net} I_{z_T}$, and the secular part of the homonuclear dipolar coupling (7) is $H_{ZZ} = \sum_{j>i}^N B_{ij}(3I_{z_i}I_{z_j} - \vec{I_i}\cdot\vec{I_j})$. The net resonance offset, $\Omega_z^{net} = \Omega_z^{ext} + \Omega_z^{loc}$, is a combination of the local offset, Ω_z^{loc} (e.g., due to sample diamagnetism, offset from the magnet's isocenter, and the chemical shift) and any external offset imposed by the experimentalist, Ω_z^{ext} (e.g., due to the applied magnetic field gradient and any pulse frequency offset). Bulk samples are similar to an ensemble of N spin clusters, each with distinct Ω_z^{net} values.

Starting at $t = 0$ (see Fig. 1A), the repeating block has three intervals: "A," "B," "C," of duration Δ, $4(\Delta + T_{90})$, and Δ, respectively, (where $\Delta + T_{90} \approx \Delta$). Nonselective, rectangular pulses (with $T_{90} \approx 0.005$ ms, $T_{180} \approx 0.010$ ms) are applied only during interval "B," in a particular pattern related to the Carr-Purcell (CP) experiment (1). Using $\{X, X\}$ as a shorthand for the CP cycle: $(\tau - 180_X - 2\tau - 180_X - \tau)$, where "$180_X$" represents a 180° rotation about the X direction and "τ" is a delay time, then Fig. 1A has the structure

$$\Delta - 90_Y - \{X, X\}90_{-X}\{-X, -X\} - \{X, X\}90_{+X}\{-X, -X\}$$
$$- 90_Y - \Delta. \tag{S1}$$

The key improvement over the first-generation sequence is that an extra $\{-X, -X\}\{X, X\}$ is inserted in the middle of interval "B," in order to double the duration of intervals "A" and "C," which now last time $\Delta = 2(2\tau + T_{180})$. The extra 90_{-X}, 90_{+X} pair is optional, but it improves the line-narrowing performance of this longer, second-generation block.

In our model (1), this pulse block causes an extreme "line-narrowing" of the MR spectrum of a solid. Specifically, if the magnetic Zeeman (H_Z) and dipolar (H_{ZZ}) parts of the spin Hamiltonian are held constant in time, then the approximate effect of the pulse block, at the time of the second dashed line ($t = 500$ ms in Fig. 1A), is described as $(H_Z + H_{ZZ})\Delta + (-H_{ZZ}/2)4\Delta + (-H_Z + H_{ZZ})\Delta = 0$. Thus, this looks like a "time-suspension" pulse sequence, over the interval between dashed lines in Fig. 1A, even in the presence of a strong applied field gradient during interval "B." This is called a quadratic echo sequence (1), because the negative dipolar evolution is due to transverse field terms proportional to $(\Omega_z^{net})^2$, which emerge from commutators in $\bar{H}_{\{\pm X, \pm X\}}^{(1)}$, once the nonzero duration of the very strong π pulses in $\{X, X\}$ and $\{-X, -X\}$ is taken into consideration (3–6).

At first glance, the burst of pulses in interval "B" of the quadratic echo pulse block in Fig. 1A may resemble earlier line-narrowing approaches to MRI of solids using MREV-8 (8–10). However, as discussed in ref. 1, the effective Hamiltonian in interval "B" is identical to the one achieved by the continuous rf irradiation interval of the magic echo pulse sequence (10–12); this means that the modulated applied field gradient (used for the MRI sequence in the next section) is effective during the much longer time intervals "A" and "C." In contrast to the magic echo, the quadratic echo works best in the regime where $H_Z \geq H_{ZZ}$; this means that applied field gradients can be left on during interval "B" without adding artifacts, and also that this method works well for spin systems with large chemical shift anisotropies or susceptibility broadening.

For the case of constant H_Z and H_{ZZ}, the signal detected stroboscopically, after every repetition of the quadratic echo pulse block, decays with a much slower than normal effective T_2 (T_{2eff}). The effects of fluctuating magnetic fields would provide an upper limit on the value of T_{2eff}. In silicon and buckyball powders (1, 5, 6), this quadratic echo approach has been used to push T_{2eff} out to $\approx \frac{1}{3}T_1$, corresponding to line-narrowing by more than a factor of 10,000. Using the same approach, we have obtained factors of $\approx$1,000 line-narrowing of the ^{31}P MR spectrum in bovine bone, in human deciduous (baby) teeth, and in lobster shell (all were ex vivo, and dry). While this is already quite good, the effective T_2 in bone has only been pushed out

to $\approx \frac{1}{3,000}T_1$ (at 12 Tesla). This suggests that further spectral (and thus, spatial) resolution enhancements are possible, if the extra terms that complicate the ^{31}P spin Hamiltonian in bone (e.g., due to nearby ^{1}H spins), could be reduced by decoupling.

Lastly, it appears that the second-generation block in Fig. 1A could be further improved upon if we could use more complicated pulse phase patterns, across multiple blocks. In practice, however, repeated application of Fig. 1A blocks yielded the best possible performance, given the software and hardware limitations of the Bruker Avance running ParaVision 3.0.1.

Using the 3D MRI Sequence to Acquire k-space Data. All images in this paper used the 3D MRI sequence depicted in Fig. 1B. The basic idea is that we first use our quadratic echo pulse block to "make the solid MR spectrum look like that of a liquid," and then we overlay schemes for MRI of liquids (13), modified for our unique requirements. Because this pulse block (Fig. 1A) "turns off" the static contributions to the ^{31}P MR linewidth (1, 5, 6), the spatial encoding of the signal (13) requires modulation of the applied field gradient (e.g., $G_z = dB_z/dz$). For example, applying $+G_z$ during intervals "A" and "B," followed by $-G_z$ during interval "C," yields an effective gradient acting over intervals "A–B–C" of $\approx \frac{2\Delta}{6\Delta}G_z = \frac{1}{3}G_z$. A pulse frequency offset (f_{offset}) is another control knob. A constant $+f_{offset}$ has no net effect over the "A–B–C" block, but flipping to $-f_{offset}$ during "C" yields a net $\approx \frac{1}{3}f_{offset}$, for the whole sample (1, 5, 6). This knob is useful for positioning the image at a particular place in the field of view (FOV).

The sequence summarized in Fig. 1B samples the 3D **k** space (13) at discrete points of a Cartesian grid. It always starts at **k** = (0, 0, 0), followed by a series of three distinct frequency-encoding steps. First, the initial gradient ($+G_z$) and offset frequency value ($+f_{offset}$) are reached, and then a nonselective, rectangular, 90° pulse is applied. Both G_z and f_{offset} are held constant through the first dashed line, so the first detected echo is an excellent "time = 0" point of the pseudo-FID, which is crucial for proper phasing (and co-adding) of the signals at this **k** = (0, 0, 0) point. Next, to map out a particular Cartesian trajectory in **k** space, just G_z is modulated during the N_z loop, then just G_y is modulated during the N_y loop, then just G_x is modulated during the N_x loop. We refer to this loop ordering as $\{Z, Y, X\}$. Note that the f_{offset} value can be different in each loop, to "center" the sample at a particular (x, y, z) of the FOV.

Taking into account the group delay of the 15-kHz low-pass filter, the echo peaks at the end of each pulse block are sampled using five complex points (dwell time of 0.002 ms), and the data is exported from the Bruker for further processing offline. After three applications of three-point binomial smoothing, the center point of each 5-point acquisition window is used to make a pseudo-FID. After phasing the time = 0 point of the complex pseudo-FID, the sign of the imaginary points in the odd-numbered windows is then flipped, to account for the "hidden 180_Y" in each pulse block (1, 5, 6). The resulting points of the pseudo-FID have a "sparse dwell time" of the total "A–B–C" block duration ($6\Delta + 4T_{90} \approx 0.5$ ms), and they oscillate due to the effective applied field gradient and f_{offset}, so this sequence is a hybrid of echo (for internal fields) and FID (for external fields) imaging approaches, which enables high spatial resolution.

Offline Processing of the k-Space Data. After data points are acquired using the Bruker Avance, processing takes place offline. The extraction of the pseudo-FIDs, the filling of **k** space, the generation of the images, including 3D surface plots and movies, made use of programs that were written using commercially available software (IgorPro 6.2, Wavemetrics). The octahedron of **k**-space data was centered in a $(64$ pt$)^3$ data cube (as in Fig. 2C), then 4x-zero-filled (or 2x- in Fig. 3 B and C), followed by 3D Fourier transformation to generate the image vs. three frequency axes (f_x, f_y, f_z). The complex image points are plotted in magnitude mode. For Fig. S3, only octant 1 of **k** space was acquired so the **k** = (0, 0, 0) point was in the lower corner of a $(32$ pt$)^3$ data cube and the complex image points were then plotted in the real mode.

Most of the three-dimensional surface plots of the ^{31}P MR images shown here (Figs. 2D, 3B, 4C and Figs. S3B and S6), are opaque isosurfaces drawn at a single magnitude value using the Gizmo XOP, an OpenGL compiler for Igor-Pro 6.2. In contrast, Fig. 5 A, C, and D and Movie S4 show three different surfaces at three different magnitude values simultaneously, using translucency. In order for Gizmo to implement the color and translucency correctly as the object is viewed from different orientations, the triangles that make

up the original isosurface are first stored in an array, which is then plotted to show the surface of interest. Each time the sample's orientation changes, the array of triangles is sorted according to their centroid distance from the viewer, in order to plot the triangles from the back to the front of the viewable volume.

Effective Gradient Size Determination. The sparse dwell time of the pseudo-FID for each dataset determines the total bandwidth (BW) in Hz (see Table S1). The bandwidth is the same for all three dimensions (i.e., the FOV in $(Hz)^3$ is isotropic). The FOV in $(Hz)^3$ can be converted to the FOV in $(meters)^3$ by dividing each frequency axis (e.g., f_z) by the corresponding gradient factor (e.g., $\alpha_z \gamma G_z / 2\pi$, where α_z is a scale factor <1, that compares the time that the gradient "is effective" to the total sparse dwell time between points of the pseudo-FID). As a first approximation, $\alpha_z = \frac{1}{3}$ if we can apply $+G_z$ during intervals "A" and "B," followed by $-G_z$ during interval "C" (see blue dotted trace in Fig. S4), because the effective gradient over the sparse dwell time is $\approx \frac{2\Delta}{6\Delta} G_z = \frac{1}{3} G_z$. Of course, the current through the gradient coils cannot change instantaneously, so a better value for α_z is obtained by measuring the output of the gradient amplifiers on a digital oscilloscope and integrating to obtain α_z (see green dashed trace in Fig. S4). An even better value for α_z takes into account the inline low-pass isolation filter (Tesch A14X29-1.2/B) located en route to the gradient coil (at the wall of the magnet room), which adds a $\approx$0.011-ms delay to the schematic gradient waveform (see the black solid trace in Fig. S4). Of course, the actual waveform is more complicated, with curvature during the ramp, overshoot at the top, and then decaying oscillations. The quantitative comparison of micro-CT data to MR images that assume our schematic model (see the next section) suggests that these high frequency oscillations may be safely ignored for our conditions. In our model, we also ignore the small displacements from the **k**-space grid that occur when one gradient component turns off, and another turns on (e.g., while switching from G_z to G_y). The measured α_i components can be slightly different for Z vs. X/Y, which leads to slight anisotropy of the spatial voxels. See Table S1 for the applied gradient amplitude, effective gradient scale factors and resultant FOV in $(meters)^3$ for each dataset used for the figures given in this paper. Note that each figure is zoomed in to the part of the full FOV that contains the image. In this implementation of Fig. 1B, the Bruker Avance spectrometer limited us to a simple repetition of the Fig. 1A blocks, which can result in artifacts whenever the image crosses the $f = 0$ or $f = \pm \frac{BW}{2}$ planes. Thus, the image size and location were controlled by our choice of the gradient magnitude, f_{offset_x}, f_{offset_y}, and f_{offset_z}, in order to minimize artifacts while optimizing spatial resolution and signal-to-noise.

Comparing ^{31}P MRI to Micro-CT Images. As a validation of our approach, the same pork rib sample that was imaged for Fig. 3 has also been studied using micro-computed tomography. Micro-CT is considered the gold standard for obtaining a 3D volumetric map of the bone mineral (14). More precisely, micro-CT measures the X-ray linear attenuation coefficient, which grows so quickly with atomic electron density ($\approx Z^4$) that the 'mineral' image is dominated by the calcium (atomic number $Z = 20$).

Fig. S5 shows 2D slices of the micro-CT data measured by a μCT 35 (Scanco Medical), using 55 kVp for the peak energy, 500 ms for the integration time, and 37 microns (isometric) for the nominal resolution/voxel size. The raw data displayed in the as-measured voxels (Fig. S5A) may be transformed into Hounsfield Units with a known linear transformation, if desired. Fig. S5B shows the effect of Gaussian broadening to match the ^{31}P MRI resolution; note how this blurs out the trabecular bone network in the marrow space. Fig. S6 shows a coregistration of our ^{31}P MRI surface plot (i.e., Fig. 3B) with a surface plot of the broadened micro-CT measurement on the same sample. They look fairly similar, but not identical, which is to be expected at this early stage. Further improvements in the spatial resolution of our technique should start to reveal local differences between these two maps (the ^{31}P MRI measures just the phosphorus, the other predominantly calcium).

Imaging Acceleration Using Sparse Sampling of k Space. While the spatial resolution demonstrated so far is encouraging, the total imaging time is quite long, due to the long T_1 of the solid samples (>30 s for ^{31}P in bone at 4 T). For example, to acquire the data for Fig. 2 required a long repetition time, $T_{rep} = \frac{8}{5} T_1$, and consequently took 47.6 hours (one scan, no signal averaging). One way to reduce scan acquisition time would be to use $T_{rep} \ll T_1$, at the cost of signal-to-noise. A second way is to extend the pseudo-FID sequence of Fig. 2 to form a pseudo-echo, which is then hit by a "flip-back" pulse (i.e., a driven equilibrium technique) (15). A third way is to apply the ideas of sparse MRI, or compressed-sampling MRI, to undersample the **k** space in a pseudo-random way (16, 17). Fig. S3 shows the compressed-sampling approach applied to the sample from Fig. 2. A small number ($N_{sparse} = 66$) of trajectories, each with 32 acquisition windows, sample octant 1 of the original octahedron in **k** space. Three different loop patterns, $\{Z, Y, X\}$, $\{Y, X, Z\}$, $\{X, Z, Y\}$, are used for each $\frac{1}{3}$ of the N_{sparse} trajectories. For each loop pattern, the (N_z, N_y, N_x) values are chosen randomly, subject to the total window number constraint. The trajectories followed are depicted in Fig. S3A, and the corresponding surface plot of the image following Fourier transformation (and 4 ×-zero-filling) is in Fig. S3B. For this case, the **k** = (0, 0, 0) point is at one corner of a 32 point **k**-space data cube, and the real part of the complex image is shown. The image in Fig. S3B was acquired in only 88 min, a dramatic improvement over the 2,856 minutes of Fig. 2D. A wide variety of strategies for compressed-sampling of **k** space, and for the subsequent image processing (16, 17), are compatible with our approach, and so further improvements upon this result will be the subject of future work.

1. Dong Y, Ramos R, Li D, Barrett SE (2008) Controlling coherence using the internal structure of hard pi pulses. *Phys Rev Lett* 100:247601.
2. Li D, Dementyev AE, Dong Y, Ramos RG, Barrett SE (2007) Generating unexpected spin echoes in dipolar solids with pi pulses. *Phys Rev Lett* 98:190401.
3. Li D, et al. (2008) Intrinsic origin of spin echoes in dipolar solids generated by strong pi pulses. *Phys Rev B Condens Matter Mater Phys* 77:214306.
4. Li D (2007) Unexpected spin echoes in dipolar solids. PhD thesis (Yale University, New Haven, CT).
5. Dong Y (2009) Effects of hard but finite pi pulses: From controlled coherence flow to extreme line-narrowing and MRI of solids. PhD thesis (Yale University, New Haven, CT).
6. Ramos RG (2010) Novel pulse sequences exploiting the effects of hard pi-pulses. PhD thesis (Yale University, New Haven, CT).
7. Slichter CP (1990) *Principles of Magnetic Resonance*, 3rd Ed., ed. Lotsch HKV (Springer, New York).
8. Miller JB, et al. (1990) Line-narrowing approaches to solid state NMR imaging: Pulsed gradients and second averaging. *Philos Trans R Soc Lond A* 333:413–426.
9. Cory DG, Miller JB, Turner R, Garroway AN (1990) Multiple-pulse methods of ^{1}H NMR imaging of solids: second-averaging. *Mol Phys* 70:331–345.
10. Demco DE, Blümich B (2000) Solid state NMR imaging methods. Part II: Line narrowing. *Concepts Magn Reson* 12:269–288.
11. Matsui S (1991) Solid-state NMR imaging by magic sandwich echoes. *Chem Phys Lett* 179:187–190.
12. Rhim W-K, Pines A, Waugh JS (1970) Violation of the spin-temperature hypothesis. *Phys Rev Lett* 25:218–220.
13. Bernstein MA, King KF, Zhou XJ (2004) *Handbook of MRI Pulse Sequences* (Elsevier Academic, Boston).
14. Genant HK, Engelke K, Prevrhal S (2008) Advanced CT bone imaging in osteoporosis. *Rheumatology* 47:iv9–iv16.
15. van Uijen CMJ (1984) Driven-equilibrium rf pulses in NMR imaging. *J Mag Reson Med* 1:502–507.
16. Lustig M, Donoho D, Pauly JM (2007) Sparse MRI: The application of compressed sensing for rapid MR imaging. *Magn Reson Med* 58:1182–1195
17. Lustig M, Donoho DL, Santos JM, Pauly JM (2008) Compressed sensing MRI. *Signal Proc IEEE* 25:72–82.
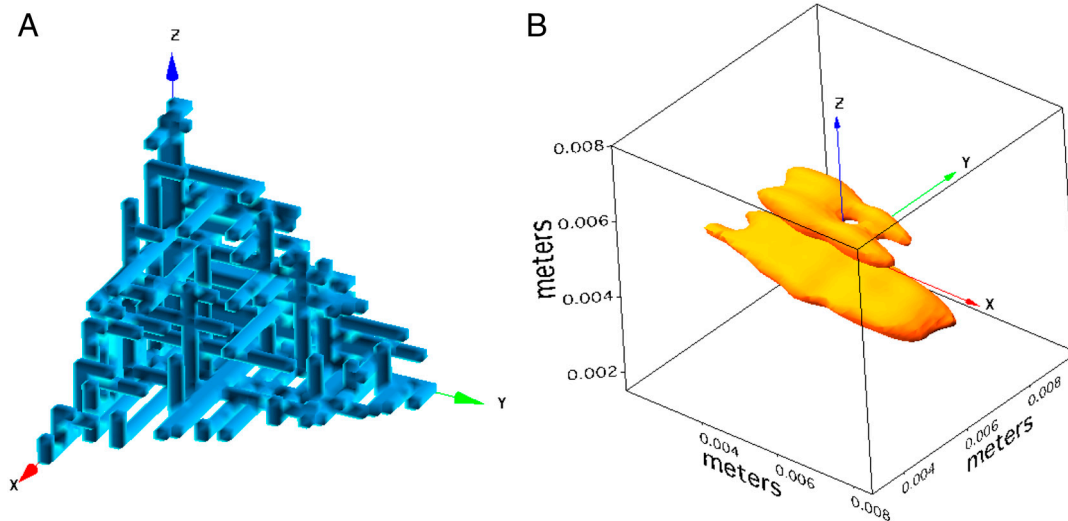
Fig. S1. Comparison of a measured solid linewidth to a typical liquid linewidth. NMR spectrum of ^{31}P in the pork rib sample (red) as measured on our 4T MRI system (Larmor frequency of 68.94 MHz, FWHM $\approx$50 ppm), in the absence of any gradients. For comparison, a Lorentzian with a 0.2 ppm FWHM (blue) is a conservative approximation of the NMR spectrum that the same system would be expected to obtain for a similar-sized water phantom. Both spectra are normalized to unit amplitude to simplify the comparison of the FWHM. (*Inset*) The main figure curves are rescaled by factors of (1/FWHM) to demonstrate the connection between linewidth and signal-to-noise ratios. This rescaling makes the area under each curve the same, which approximates what one would expect if measuring two samples containing the same number of ^{31}P and ^{1}H spins.

Fig. S2. Estimated number of ^{31}P nuclei in a "typical" 20-μm human cell. (*A*) The estimated number of ^{31}P in membranes, by location (1). The blue dashed line is the estimated number (2) of ^{31}P in DNA and RNA ($\approx$2 × 10^{10}). (*B*) The sum of all parts in *A* is the total number of ^{31}P in membranes (red bar) for typical cell ($\approx$5.5 × 10^{11}), which is more than a factor of three times the ^{31}P content measured in brain metabolites (green bar) (3). An independent estimate of the brain membrane ^{31}P content (green circle) (3) is consistent with ours. As comparisons, the ^{1}H content of mobile water in the cell (1) is $\approx$9 × 10^{13}, which matches the ^{31}P content of the same amount of bone mineral.

1. Frietas R (1999) *Nanomedicine*, Vol. I: Basic Capabilities (Landes Bioscience, Georgetown, TX), pp. 256, Table 8.17.
2. Sterner RW, Elser JJ (2002) *Ecological Stoichiometry: The Biology of Elements from Molecules to the Biosphere* (Princeton Univ Press, Princeton, NJ).
3. Buchli R, Duc CO, Martin E, Boesiger P (1994) Assessment of absolute metabolite concentrations in human tissue by 31P MRS in vivo. Part 1: Cerebrum, cerebellum, cerebral gray and white matter. *Magn Reson Med* 32:447–452.

Fig. S3. Sparse **k**-space mapping and the resulting image of the dry bovine bone sample. (*A*) Depiction of the 66 randomly chosen sparse trajectories taken through **k** space to produce a sparse image. The three different loop patterns, {*Z, Y, X*}, {*Y, X, Z*}, and {*X, Z, Y*} were used equally amongst the sparse trajectories. The loop pattern {*Z, Y, X*} means after starting at **k** = (0, 0, 0) we map N_z points in the k_z-direction, then N_y points in the k_y-direction and N_x points in the k_x-direction. For each loop pattern, (N_x, N_y, N_z) were chosen randomly subject to the constraint that $N_x + N_y + N_z = 31$ so that there are a total number of 32 acquisition points per trajectory. (*B*) The resulting image of the same sample imaged in Fig. 2 by taking the Fourier transform of the sparsely sampled **k** space. The isosurface value is 57% the maximum signal value. The imaging time was 88 min, compared to 47 h for the dense sampling image in Fig. 2. The "smearing" of the image is due to our pseudo-random sampling of **k**-space oversampling the $k_x = 0$, $k_y = 0$, and $k_z = 0$ planes compared to the rest of **k** space.
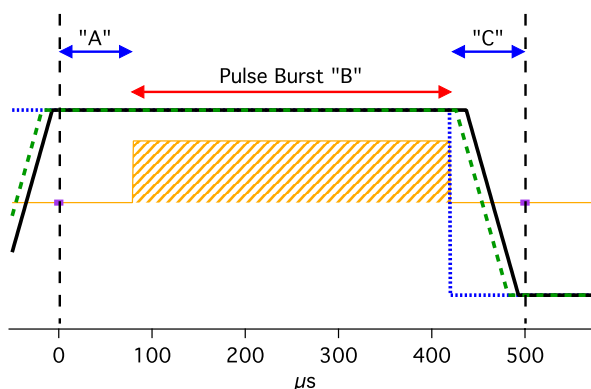

Fig. S4. A schematic of the gradient transient. For best results, the gradient should be constant during "B," and during each 10-μs data acquisition window (the small purple rectangles at the beginning of "A" and the end of "C"). Ideally the gradient transient would be like the dotted blue line and switch instantaneously immediately after the pulse burst "B." A better approximation of the gradient transient is given by the dashed green line where there is some delay before the gradient transient starts (approximately 6 μs) after it is called, and there is also some time for the gradient ramp to take place (<56 μs for the "ramp-off" mode and small gradient amplitudes we use in this paper, see Table S1). An even better model for the gradient transient takes into account the gradient low-pass isolation filter through which the current flows before arriving at the gradient coils. This adds an extra 11-μs delay and is given by the black solid line. This is the final model used to calculate the effective gradient factors for scaling the images presented here (see Table S1).
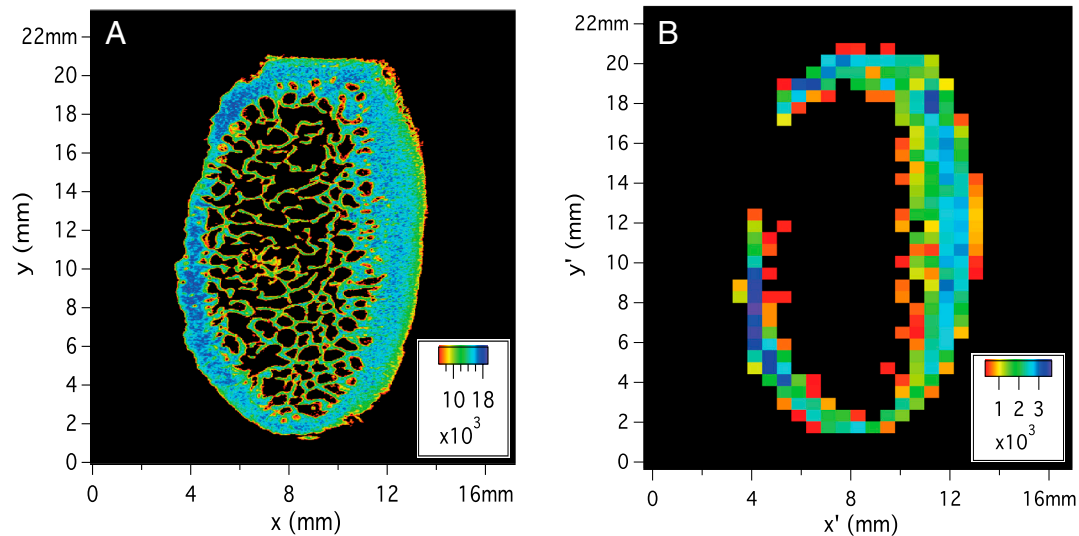
Fig. S5. Two-dimensional slice of micro-CT image of the wet pork rib sample, before and after Gaussian broadening. (*A*) A 2D slice (0.037-mm thick) of the micro-CT data measured in the wet pork rib in PBS using a Scanco Medical "μCT 35" in the Yale Core Center for Musculoskeletal Disorders. The 2D resolution is $(0.037 \text{ mm})^2$. (*B*) The same slice of micro-CT data shown in Fig. S5*A* now Gaussian-broadened to match the digital resolution of our MRI images for comparison. The 2D resolution is now $(1.184 \text{ mm})^2$, but the pixels shown are $(0.592 \text{ mm})^2$ and the slice thickness is 0.592 mm. The cortical bone ring appears thinner on the left edge (and thicker on the right edge) because the bone is rotated slightly relative to the slicing plane.
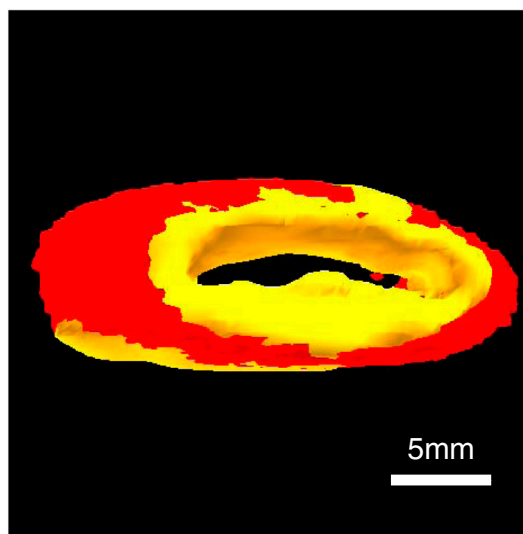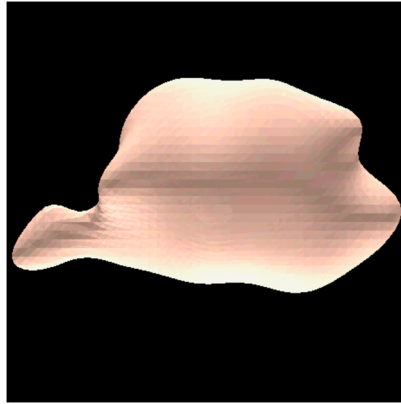

Fig. S6. Isosurface rendering of the Gaussian-broadened 3D micro-CT data (red) registered with our ^{31}P MRI data (yellow) as shown in Fig. 3*B*. The isosurface value chosen for the micro-CT data is 10% of the maximum signal value, while for the ^{31}P MRI data the isosurface value is 33% of the maximum signal value, and shows the thick cortical bone ring of the wet pork rib.

Movie S1. A movie illustrating the **k**-space mapping that is shown in Fig. 2*A* and *B*.

Movie S1 (MOV)

Movie S2. A movie giving a better view of the isosurface rendering of the dry bovine bone sample depicted in Fig. 2*D*.

Movie S2 (MOV)

Movie S3. A movie giving a better view of the isosurface rendering of the pork rib sample depicted in Fig. 3*B*.

Movie S3 (MOV)

Movie S4. A movie giving a better view of the three different isosurface renderings of the mouse brain sample depicted in Fig. 5 *A*, *C*, and *D*.
Movie S4 (MOV)

Table S1. Relevant parameters for MRI images shown in this paper

	Fig. 2	Fig. 3 *B* and *C*	Fig. 4*C–J*	Fig. 5	Fig. S2
G (mT/m)	30	7.5	18	7.5	30
$\alpha_{x/y}$	0.146	0.180	0.189	0.172	0.146
α_z	0.178	0.181	0.205	0.173	0.178
Δ (ms)	0.0776	0.0896	0.092	0.084	0.0776
T_{rep} (s)	80	30	30	4.2	80
NA	1	2	4	36	1
FOV (Hz^3)	2,070 ×	1,763 ×	1,712 ×	1,894 ×	2,070 ×
(isotropic)	2,070 ×	1,763 ×	1,712 ×	1,894 ×	2,070 ×
	2,070	1,763	1,712	1,894	2,070
FOV (m^3)	0.027 ×	0.076 ×	0.029 ×	0.085 ×	0.027 ×
($x \times y \times z$)	0.027 ×	0.076 ×	0.029 ×	0.085 ×	0.027 ×
	0.022	0.075	0.027	0.085	0.022

Includes the gradient magnitude (*G*), the effective gradient scale factors used (α_i), the duration of interval "A" (or "C") in the Fig. 1*A* block (Δ), the repetition time (T_{rep}), the number of acquisitions averaged together (NA), and the measured field-of-view (FOV) in Hertz^3 and meters^3.